

Optical simulation of $CsPbI_3$/TOPCon tandem solar cells with advanced light management

Min Yue(岳敏), Yan Wang(王燕), Hui-Li Liang(梁会力), and Zeng-Xia Mei(梅增霞)
Citation: Chin. Phys. B, 2022, 31 (**8**): 088801. DOI: 10.1088/1674-1056/ac693d
Journal homepage: http://cpb.iphy.ac.cn; http://iopscience.iop.org/cpb

What follows is a list of articles you may be interested in

Reveal the large open-circuit voltage deficit of all-inorganic$CsPbIBr_2$ perovskite solar cells

Ying Hu(胡颖), Jiaping Wang(王家平), Peng Zhao(赵鹏), Zhenhua Lin(林珍华), Siyu Zhang(张思玉), Jie Su(苏杰), Miao Zhang(张苗), Jincheng Zhang(张进成), Jingjing Chang(常晶晶), and Yue Hao(郝跃)
Chin. Phys. B, 2022, 31 (**3**): 038804. DOI: 10.1088/1674-1056/ac464b

Charge transfer modification of inverted planar perovskite solar cells by NiO_x/Sr:NiO_x bilayer hole transport layer

Qiaopeng Cui(崔翘鹏), Liang Zhao(赵亮), Xuewen Sun(孙学文), Qiannan Yao(姚倩楠), Sheng Huang(黄胜), Lei Zhu(朱磊), Yulong Zhao(赵宇龙), Jian Song(宋健), and Yinghuai Qiang(强颖怀)
Chin. Phys. B, 2022, 31 (**3**): 038801. DOI: 10.1088/1674-1056/ac1fda

High efficiency ETM-free perovskite cell composed of CuSCN and increasing gradient $CH_3NH_3PbI_3$

Tao Wang(汪涛), Gui-Jiang Xiao(肖贵将), Ren Sun(孙韧), Lin-Bao Luo(罗林保), and Mao-Xiang Yi(易茂祥)
Chin. Phys. B, 2022, 31 (**1**): 018801. DOI: 10.1088/1674-1056/ac0bb0

Stabilization of formamidinium lead iodide perovskite precursor solution for blade-coating efficient carbon electrode perovskite solar cells

Yu Zhan(占宇), Weijie Chen(陈炜杰), Fu Yang(杨甫), and Yaowen Li(李耀文)
Chin. Phys. B, 2021, 30 (**8**): 088803. DOI: 10.1088/1674-1056/abfbcb

Influence of CdS films synthesized by different methods on the photovoltaic performance of CdTe/CdS thin film solar cells

Jun Wang(汪俊), Yuquan Wang(王玉全), Cong Liu(刘聪), Meiling Sun(孙美玲), Cao Wang(王操), Guangchao Yin(尹广超), Fuchao Jia(贾福超), Yannan Mu(牟艳男), Xiaolin Liu(刘笑林), Haibin Yang(杨海滨)
Chin. Phys. B, 2020, 29 (**9**): 098802. DOI: 10.1088/1674-1056/abad22

Optical simulation of $CsPbI_3$/TOPCon tandem solar cells with advanced light management

Min Yue(岳敏)[1,2,3], Yan Wang(王燕)[1,2,†], Hui-Li Liang(梁会力)[1,2], and Zeng-Xia Mei (梅增霞)[1,2,‡]

[1] *Beijing National Laboratory for Condensed Matter Physics, Institute of Physics, Chinese Academy of Sciences, Beijing* 100190, *China*
[2] *Songshan Lake Materials Laboratory, Dongguan* 523808, *China*
[3] *School of Physical Sciences, University of Chinese Academy of Sciences, Beijing* 100049, *China*

(Received 16 March 2022; revised manuscript received 14 April 2022; accepted manuscript online 22 April 2022)

Monolithic perovskite/Si tandem solar cells (TSCs) have experienced rapid development in recent years, demonstrating its potential to exceed the Shockley–Queisser limit of single junction Si solar cells. Unlike typical organic-inorganic hybrid perovskite/silicon heterojunction TSCs, here we propose $CsPbI_3$/TOPCon TSC, which is a promising architecture in consideration of its pleasurable thermal stability and good compatibility with current PERC production lines. The optical performance of $CsPbI_3$/TOPCon TSCs is simulated by the combination of ray-tracing method and transfer matrix method. The light management of the $CsPbI_3$/TOPCon TSC begins with the optimization of the surface texture on Si subcell, indicating that a bifacial inverted pyramid with a small bottom angle of rear-side enables a further minimization of the optical losses. Current matching between the subcells, as well as the parasitic absorption loss from the front transparent conductive oxide, is analyzed and discussed in detail. Finally, an optimized configuration of $CsPbI_3$/TOPCon TSC with a 31.78% power conversion efficiency is proposed. This work provides a practical guidance for approaching high-efficiency perovskite/Si TSCs.

Keywords: perovskite/Si tandem solar cells, simulation, TOPCon, $CsPbI_3$

PACS: 88.40.H–, 88.40.hj, 84.60.Jt **DOI:** 10.1088/1674-1056/ac693d

1. Introduction

Crystalline silicon (c-Si) solar cells have occupied over 90% photovoltaic market due to their low cost, high efficiency and mature industrialization. The power conversion efficiency (PCE) of current world record cell for single-junction c-Si solar cells is 26.7% which is close to the 29.4% efficiency limit of Si.[1,2] In order to break through this efficiency ceiling, one approach is to fabricate multi-junction solar cells which can effectively enhance the utilization of the solar spectrum by reducing the thermalization loss. The theoretical efficiency of Si based two-junction solar cells can exceed 45% which is quite attractive.[3] The calculation result manifests that Si ($E_g = 1.12$ eV) based TSC requires an absorption material with $E_g \sim 1.70$ eV in the top cell so as to maximize the efficiency.[3] Halide perovskites with tunable bandgap (1.5 eV–2.3 eV), high absorption coefficient and good defect tolerance,[4,5] have rapidly enhanced the PCE from 3.8% to 25.7% in the last ten years.[6,7] The bandgap of perovskite can be ideally adjusted to 1.67 eV–1.75 eV by changing the composition of ABX_3.[8]

It is quite incredible that the PCE of perovskite/Si (PVK/Si) TSCs has developed extremely fast, from 13.7% in 2015[9] to 29.8% in 2021,[10] exceeding that of the c-Si solar cells. In high-efficiency PVK/Si TSCs, silicon heterojunction (SHJ) solar cell is usually chosen as the bottom cell because of its high PCE and high open-circuit voltage (V_{oc}).[11] However, the SHJ totally distinguishes from the mainstream passivated emitter and rear cell (PERC), leading to a quite high levelized cost of electricity (LCOE). The tunnel oxide passivated contact (TOPCon) silicon solar cell is another outstanding candidate for the bottom Si solar cell which is compatible better with existing PERC production lines and has manifested a high record efficiency of 26.0%.[12] The LCOE of PVK/TOPCon TSCs has been calculated to be lower than PVK/SHJ TSCs for both utility and residential installation by Fraunhofer ISE.[13] Currently, the researches of PVK/Si TSCs mainly focus on organic-inorganic hybrid perovskite due to its relatively high efficiency. However, its thermal stability is still a huge challenge.[14] On the other hand, the all inorganic perovskite $CsPbI_3$ has been demonstrated to be more superior thermal stability and incredibly increased PCE from 2.9% to 20.37% in 6 years.[15,16] Meanwhile, the optimal bandgap of $CsPbI_3$ is 1.72 eV,[17] which is suitable for the application of PVK/Si TSCs.

To further improve the PCE of PVK/Si TSCs, one effective way is to reduce optical loss by employing light trapping structures. Upright pyramid structure is the most common texture in silicon solar cells, and achieved by etching silicon wafer in a mixed alkali solution.[18] In the PVK/Si TSCs, the upright pyramid structure is usually employed in rear side of silicon solar cell while the front side is polished because of the difficulty in obtaining uniform perovskite film by spin coating on textured surface.[19,20] However, the front planar sur-

†Corresponding author. E-mail: ywang16@iphy.ac.cn
‡Corresponding author. E-mail: zxmei@iphy.ac.cn

© 2022 Chinese Physical Society and IOP Publishing Ltd

face of silicon results in poor light tapping capability. In order to cope with this challenge, upright pyramidal polydimethylsiloxane (PDMS) structure has been introduced on the top of TSCs.[21] Micrometer-thick perovskite top cell was spin-coated on fully upright pyramidal textured silicon solar cell to avoid shunt paths.[20] Double-side-textured silicon cell with sub-micrometer pyramids was employed in order to minimize the thickness of perovskite film by solution process.[22] Furthermore, the inverted pyramid structure was proposed as a more promising texture, which has a lower reflectivity than upright pyramid.[23,24] It was introduced into the PVK/Si TSC by adding an inverted pyramidal PDMS antireflective coating, which would complicate the fabrication process.[25] Directly texturing on Si seems a more practical approach to mass production.[26] Nevertheless, such a research is still relatively limited, and more attention should be paid to realizing the application of such an excellent texture to PVK/Si TSC.

Herein, we design the optics of $CsPbI_3$/TOPCon TSCs based on optical simulation that combines transfer matrix method (TMM) with ray-tracing method. The optical losses of different surface structures of silicon bottom solar cells such as rear-side upright pyramid (r-UP), bifacial upright pyramid (b-UP), and bifacial inverted pyramid (b-IP), are systematically discussed. In order to further optimize the surface structure of silicon, the dependence of optical loss on the bottom angle of rear-side b-IP is investigated particularly. Meanwhile, the photogenerated current densities of TSCs are calculated by varying the thickness of $CsPbI_3$ layer and Si bulk considering the fact that the current density matching is a key issue in two-terminal TSCs. Moreover, through comparing the optical performances of various transparent conductive oxide (TCO) layers, we find the hydrogenated indium oxide (IO:H) a more attractive front TCO candidate. Finally, the PCE of the $CsPbI_3$/TOPCon TSC can achieve 31.78% when the best matched current density is realized.

2. Device simulation parameters

The sketches of $CsPbI_3$/TOPCon TSCs with various textures are shown in Fig. 1. The material, function, and thickness of each layer are listed in Table 1 (their refractive indexes and extinction coefficients can be found in Fig. S1 in Supporting information. Both upright pyramid and inverted pyramid are 2-μm wide with an angle of 54.7°, consistent with our previous experimental data.[23] As the thickness of SiO_x layer is extremely thin ($\sim$ 1.5 nm), its influence can be reasonably ignored during the optical simulation. The rear and front ITO electrodes possess an identical carrier concentration of 2.0×10^{20} cm^{-3} in that too high carrier concentration will result in high free carrier absorption at long wavelengths. The interlayer ITO has a carrier concentration of 4.9×10^{20} cm^{-3} for the sake of favorable charge transfer between the subcells.[27]

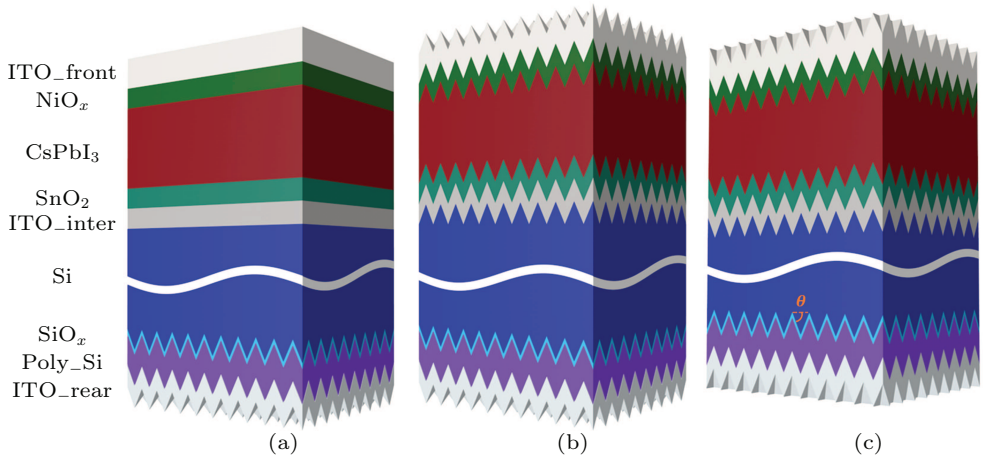


Fig. 1. Simulated structures of PVK/Si TSCs, showing (a) rear upright pyramid textured, (b) bifacial upright pyramid textured. and (c) bifacial inverted pyramid textured.

Table 1. List of simulation parameters.

Material	Function	Thickness	Reference
ITO_front	front electrode	100 nm	[28,29]
NiO_x	hole transport layer	20 nm	[30]
$CsPbI_3$	light absorption layer	1000 nm	[31]
SnO_2	electron transport layer	20 nm	[28,32]
ITO_inter	interlayer	20 nm	[28,29]
Si	light absorption layer	180 μm	[33]
Poly_Si	selective contact layer	100 nm	[13,34]
ITO_rear	rear electrode	70 nm	[13,29]

The optical properties of the $CsPbI_3$/TOPCon TSCs were simulated by the widely used ray-tracing method and TMM for the Si thick layer and other thin layers, respectively.[35] The origin code of simulation can be acquired from website.[36] The normal incidence AM1.5G spectrum (from 300 nm to 1200 nm in steps of 10 nm) was chosen as the illuminant. In order to calculate the photogenerated current density, the internal quantum efficiency (IQE) was assumed to be 100%. Thus, the photogenerated current density could be determined by integrating the photon flux of the AM1.5G solar spectrum

with the corresponding absorptance, expressed as the following equation:[32]

$$J_{\mathrm{G_i}} = -e \int_{300\ \mathrm{nm}}^{1200\ \mathrm{nm}} A_{\mathrm{i}}(\lambda)\, \Phi_{\mathrm{AM1.5G}}(\lambda)\, \mathrm{d}\lambda, \tag{1}$$

where $J_{\mathrm{G_i}}$ denotes the photogenerated current density corresponding to the absorption layer i, e is the elementary charge, λ is the wavelength, $A_{\mathrm{i}}(\lambda)$ is the absorptance of layer i as a function of λ, $\Phi_{\mathrm{AM1.5G}}(\lambda)$ is the photon flux according to the AM1.5G spectrum.

2.1. Textures

In order to figure out what kind of texture is more beneficial for the improvement of optical performance, three $CsPbI_3$/TOPCon TSCs with different silicon textures were constructed. As shown in Fig. 1(a), the Si bottom cell is r-UP textured, which is widely used in high-efficiency PVK/Si TSCs in view of its compatibility with the spin coating process.[37] Since bifacial texture is believed to be more superior in improving the optical performance,[38] two kinds of bifacial textures are compared, namely b-UP and b-IP (Figs. 1(b) and 1(c)). Figures 2(a)–2(c) display the absorptance of $CsPbI_3$ thin film and Si bulk, as well as the reflectance and transmittance of TSCs, which were simulated by incorporating the ray-tracing and TMM. The photogenerated current density of $CsPbI_3$ ($J_{\mathrm{G_CsPbI_3}}$) and Si ($J_{\mathrm{G_Si}}$), and the lost current density triggered by reflection (J_{R}) and transmission (J_{T}) as well, were calculated according to Eq. (1), and the results are shown in Fig. 2(d). It can be clearly seen that the $CsPbI_3$ layer absorbs the light in the wavelength range from 300 nm to 720 nm due to its bandgap energy (718 nm) while the Si absorbs the light in a wave length range of 600 nm–1200 nm, indicating that the $CsPbI_3$ layer with a thickness of 1000 nm can absorb most of the light below 600 nm. Compared with the single-side rear textured TSC, the bifacial textured counterparts immensely enhance the absorption of both $CsPbI_3$ layer and Si bulk. Introducing pyramidal texture in the front of Si enables the $J_{\mathrm{G_CsPbI_3}}$ to significantly increase from 16.13 mA/cm^2 to 19.07 mA/cm^2. Note that the $CsPbI_3$ layer on the top of pyramid structure will conformably repeat the pyramid feature if fabricated by an appropriate method, making the reflectivity greatly reduced (Fig. 2(b)). An ignorable lowered absorption of Si in the wavelength region from 1020 nm to 1200 nm occurs in both b-UP and b-IP, due to the dramatically increased transmittance and unequally reduced reflectance.

When the bifacial upright pyramid texture is replaced by inverted pyramid, the $J_{\mathrm{G_CsPbI_3}}$ and $J_{\mathrm{G_Si}}$ further increase by 0.16 mA/cm^2 and 0.40 mA/cm^2, respectively. The inverted pyramid texture has a desirable capability to minimize the reflectivity of the TSC, which is attributed to the increased triple bounce of incident light in the whole wavelength range from 300 nm to 1200 nm.[23] Moreover, the transmission of the light above 1000 nm can be partly suppressed, leading the $J_{\mathrm{G_Si}}$ to increase more than $J_{\mathrm{G_CsPbI_3}}$.

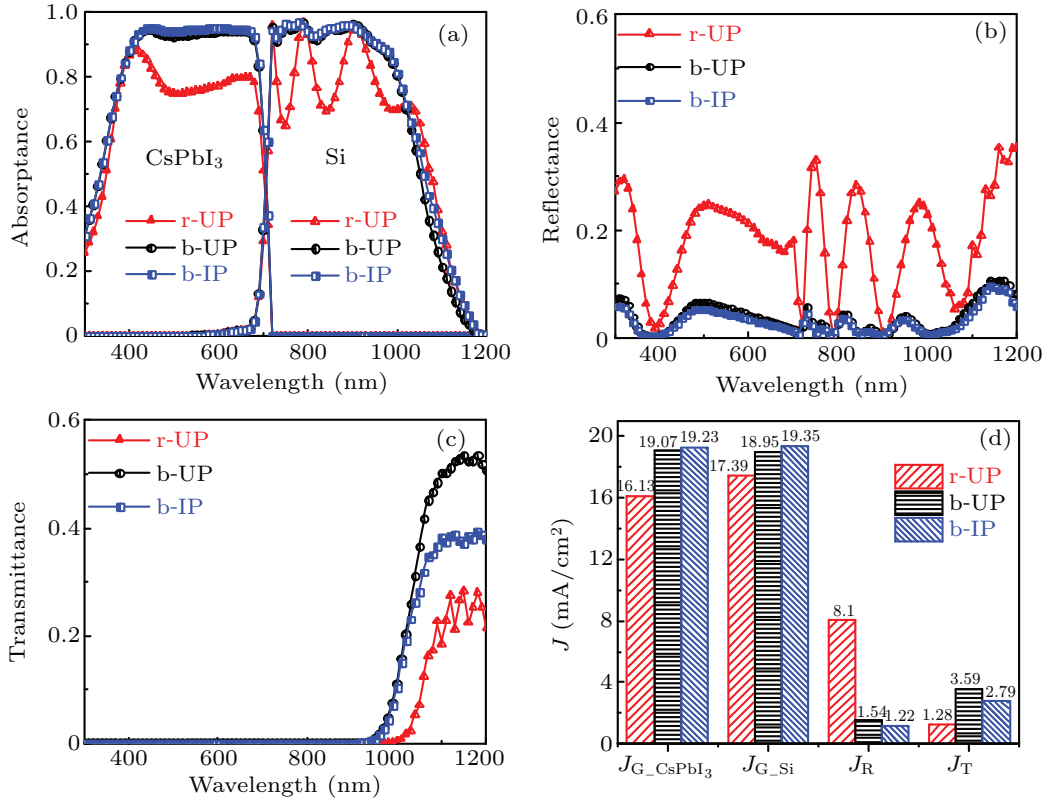


Fig. 2. Optical properties of $CsPbI_3$/TOPCon TSCs with three different textures, showing (a) absorptance of $CsPbI_3$ layer and Si bulk, (b) reflectance of TSCs, (c) transmittance of TSCs, and (d) current densities of absorbed or lost lights (in units mA/cm^2).

2.2. Bottom angle of rear-side inverted pyramid

In Subsection 2.1, we have proved that b-IP texture is a better option for PVK/Si TSC when considering the optical property. In order to further improve the optical performance of the TSCs, we discuss the influence of the bottom angle (θ) of rear-side inverted pyramid on the minimization of optical loss as shown in Fig. 1(c). Our previous work indicated that the b-IP texture with a small θ in a range of 10.0°–20.0° can improve the optical gain of PERC compared with the quintessential 54.7°.[39] The mass producible inverted pyramid structure fabricated by Cu-assisted chemical etching is usually bifacial texture.[40] On the other hand, θ can be gradually reduced by controllable single-side etching in $HF/HNO_3/H_2O$ mixture,[39] which guarantees that the following simulation of the inverted pyramid textured TSCs with θ varying from 0.0° to 54.7° is instructive and practicable.

Figures 3(a) and 3(b) show the $J_{G_CsPbI_3}$, J_{G_Si}, J_R, and J_T varying with angle θ. Obviously, $J_{G_CsPbI_3}$ basically keeps constant around 19.23 mA/cm^2 in the whole range of θ, while J_{G_Si}, changes much complicatedly. As θ increases, the optical losses from reflection and transmission are quite opposite, while the transmission is more dependent on θ. According to Figs. 3(c) and 3(d), as the 1000-nm $CsPbI_3$ layer and 180-μm Si bulk are thick enough to absorb most of the light below 930 nm, θ only influences the reflection and transmission of the wavelength above 930 nm which cannot be absorbed by $CsPbI_3$ layer. In this case, the absorption curves of $CsPbI_3$ layers with θ values of 0.0°, 10.0°, and 54.7° are almost overlapped as seen in Fig. 3(e), meaning that the $J_{G_CsPbI_3}$ is independent of the rear side texture of Si.

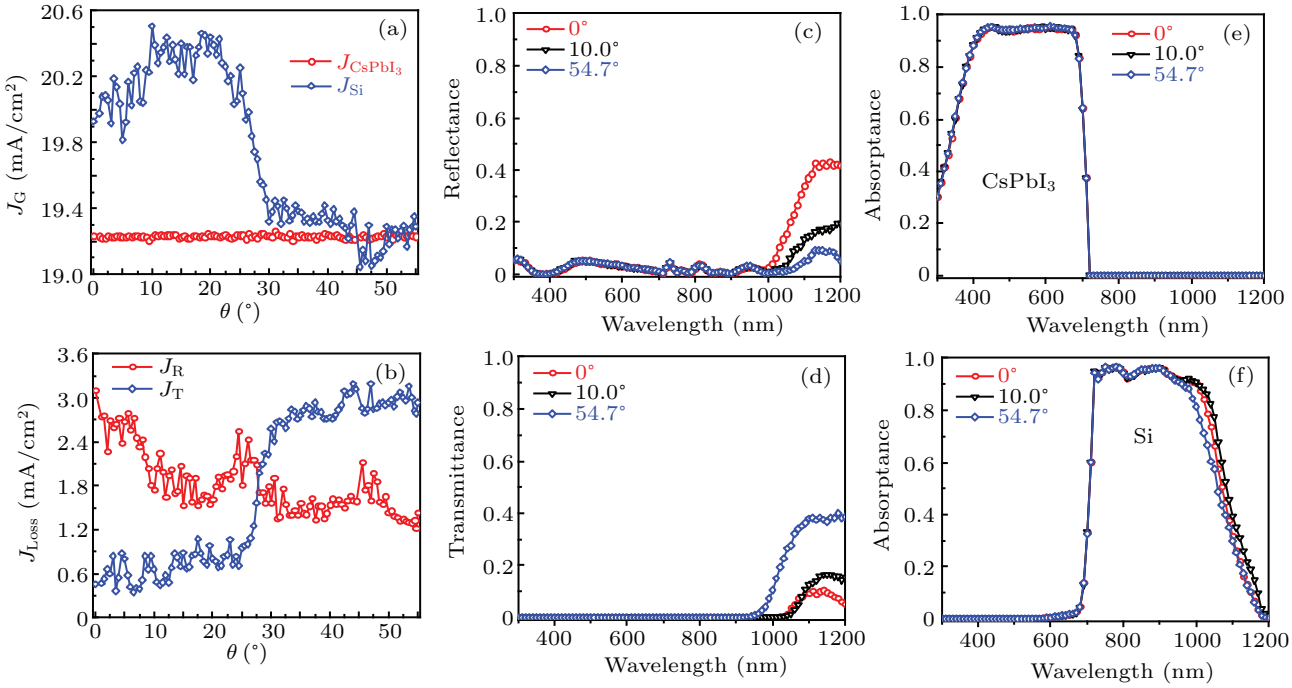


Fig. 3. (a) Photogenerated current density of $CsPbI_3$ layer and Si bulk with respect to θ; (b) current density loss of TSC triggered by reflection and transmission *versus* θ; (c) wavelength-dependent reflectance, and (d) transmittance of TSC for different values of θ; absorptance of (e) $CsPbI_3$ layer and (f) Si bulk for different values of θ.

Unlike the absorption of the $CsPbI_3$ layer, the absorption of Si bulk depends heavily on θ (Fig. 3(f)) since the changed part of wavelength in reflectivity and transmission spectrum by varying θ can be absorbed by Si bulk as shown in Fig. 3(f). The J_{G_Si} gradually increases from 19.93 mA/cm^2 to 20.43 mA/cm^2 when θ rises from 0.0° to 21.5°, then abruptly drops to 19.32 mA/cm^2 as θ increases to 30.0°, and finally gently fluctuates to 19.35 mA/cm^2 when θ turns to typical 54.7°. When $\theta \leq 25.0°$, the transmission loss J_T swings up slightly while the reflection loss J_R decreases by varying degrees. In consequence, J_{G_Si} generally gains an increase in this angle range. Especially for θ between 10.0° and 21.5°, both the J_T and J_R are relatively low, contributing to a relatively high J_{G_Si}. In a range of $25.0° < \theta < 30.0°$, the transmission loss aggravates rapidly, leading J_{G_Si} to decrease rapidly. The variation of J_T and J_R become comparatively gentle after the angle exceeds 30.0°. However, the decrease in reflectivity is not sufficiently enough to compensate for the gradually increasing transmittance, leading J_{G_Si} to decrease slowly . The maximum of J_{G_Si} can reach to 20.51 mA/cm^2 with a small θ (10.0°), which is 2.9% higher than in the planar and even 6.0% higher than the as-etched inverted pyramid. The main reason why a small θ has the ability to minimize the optical loss can be that the total internal reflection possibly happens at the top and bottom interface of TSCs on the way of light incident from TSCs to the air. According to the Snell's law, when the light comes from Si to the air, the relationship between the incident angle and the refraction angle at each interface can be

expressed as the following formula:[41]

$$n_{\mathrm{Si}} \sin \alpha_{\mathrm{Si}} = n_{\mathrm{j}} \sin \alpha_{\mathrm{j}} = n_0 \sin \alpha_0, \tag{2}$$

where n_{Si} and α_{Si} are the refractive index and incident angle of Si, n_{j} and α_{j} are the refractive index and incident/refraction angle of the layer j between Si and air, n_0 and α_0 are the refractive index and refraction angle of the air, respectively. In other words, the incident angle in Si for the total internal reflection at the top or bottom interface of TSCs only depends on n_{Si} and n_0. Our previous work have illustrated that when $\theta > 4°$, the reflection in the front interface of TSCs will generally decrease with the increase of θ because of the enhanced probability of total internal reflection; when $\theta < 24°$, the transmission in the rear interface of TSC will be suppressed for the same reason.[39]Therefore, a small θ can make a trade-off between reflection and transmission, contributing to a higher $J_{\mathrm{G_Si}}$. Thus, in order to maximize the optical harvest in PVK/Si TSCs, the rear side texture should become smoother, which will be simultaneously beneficial to the passivation of the rear-side surface of Si subcell.

2.3. Thickness of $CsPbI_3$ layer and Si bulk

Current density matching between the top subcell and bottom subcell is one of the most critical issues in two-terminal TSCs. In order to maximize the series current density of the $CsPbI_3$/TOPCon TSCs, the thickness value of $CsPbI_3$ layer and Si bulk should be delicately modulated to achieve a positive match. Asymmetrical b-IP with a bottom angle 10° of rear-side was chosen for the texture of Si subcell in this subsection. The thickness of $CsPbI_3$ layer varies from 400 nm to 2200 nm in steps of 20 nm, while the Si bulk's ranges from 40 μm to 210 μm in steps of 10 μm.

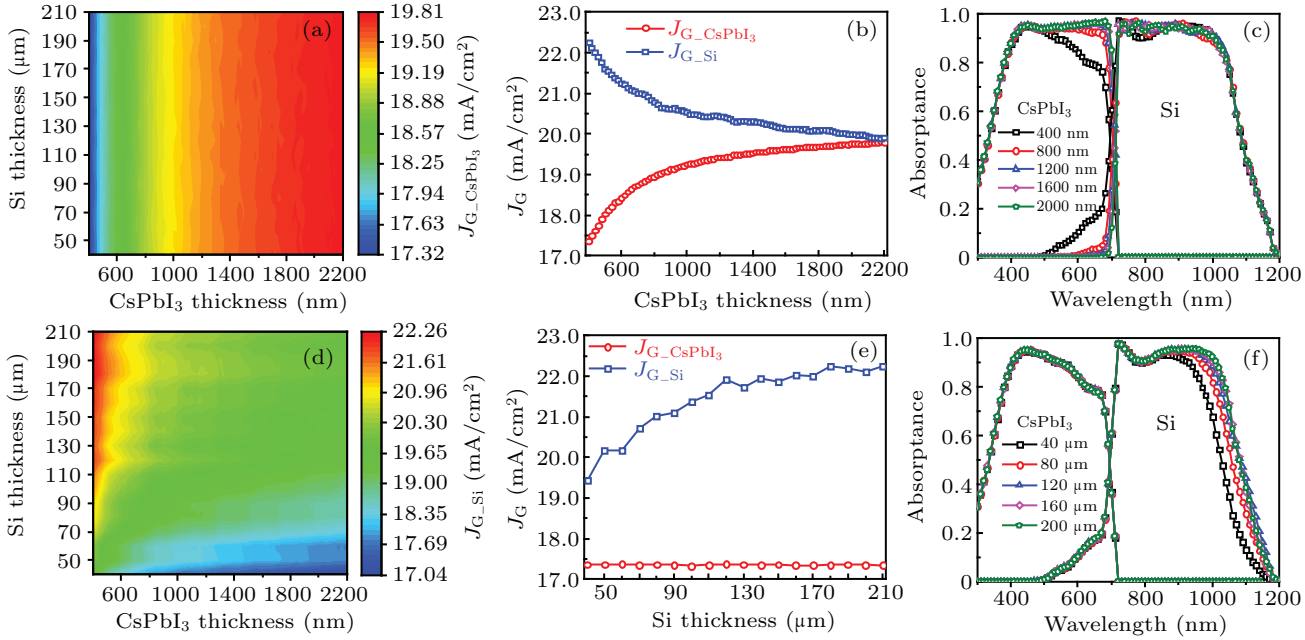


Fig. 4. Simulated optical performances of $CsPbI_3$/TOPCon TSCs with different values of thickness of $CsPbI_3$ layer and Si bulk. (a) Photogenerated current density of $CsPbI_3$ layer; (b) $J_{\mathrm{G_CsPbI_3}}$ and $J_{\mathrm{G_Si}}$, with Si bulk thickness fixed at 180 μm; (c) absorption spectrum of $CsPbI_3$ layer and Si bulk, with thickness of Si bulk fixed at 180 μm but thickness of $CsPbI_3$ layer varied; (d) photogenerated current density of Si bulk; (e) $J_{\mathrm{G_CsPbI_3}}$ and $J_{\mathrm{G_Si}}$, with thickness of $CsPbI_3$ layer fixed at 400 nm; (f) absorption spectra of $CsPbI_3$ layer and Si bulk, with thickness of $CsPbI_3$ layer fixed at 400 nm but thickness of Si bulk varied.

Figure 4(a) displays the calculated $J_{\mathrm{G_CsPbI_3}}$ as a function of both $CsPbI_3$ layer and Si bulk thickness. Obviously, the thickness of bottom Si has no significant influence on $J_{\mathrm{G_CsPbI_3}}$. Since the perovskite subcell is on the top of the TSC, $J_{\mathrm{G_CsPbI_3}}$ mainly depends on the thickness of $CsPbI_3$ layer. With the increase of $CsPbI_3$ thickness, $J_{\mathrm{G_CsPbI_3}}$ first grows rapidly and then slowly approaches to saturation (Fig. 4(b)). The maximum $J_{\mathrm{G_CsPbI_3}}$ can reach to 19.79 mA/cm^2 when the thickness of $CsPbI_3$ layer rises to 2180 nm. As shown in Fig. 4(c), owing to the high absorption coefficient of $CsPbI_3$, 400-nm-thick $CsPbI_3$ layer can adequately absorb the light in a range from 300 nm to 500 nm, but is insufficient for the light above 500 nm. When the thickness of $CsPbI_3$ layer increases to 1200 nm, it will absorb most of the light with wavelength shorter than 690 nm. With the further increase of $CsPbI_3$ layer thickness, the light in this region could be mostly absorbed.

On the contrary to the $J_{\mathrm{G_CsPbI_3}}$, the $J_{\mathrm{G_Si}}$ heavily relies on not only the thickness of Si bulk but also the thickness of $CsPbI_3$ layer, specifically for the light below 720 nm. With the $CsPbI_3$ layer thickness increasing from 400 nm to 2200 nm, $J_{\mathrm{G_Si}}$ first decreases quickly and then shows a slow-down trend (Fig. 4(d)). When the thickness of $CsPbI_3$ layer is smaller than 1200 nm, the thinner the $CsPbI_3$ layer, the more the light in the wavelength range between 500 nm and 720 nm escapes

from $CsPbI_3$ layer and then is absorbed by Si bulk. As the thickness of $CsPbI_3$ layer grows more than 1200 nm, the vast majority of light in this region is already adequately absorbed by $CsPbI_3$ layer, thus having a lower influence on J_{G_Si}. On the other hand, the thickness of Si bulk gives rise to a positive influence on the J_{G_Si} (Fig. 4(e)). As can be observed in Fig. 4(f), even 40-μm-thick Si layer is thick enough to completely absorb the escaped light (500 nm–720 nm) from the $CsPbI_3$ layer. The thickness of Si bulk primarily determine the absorption of near-infrared light. The thicker the Si bulk is, the less the optical loss in this region will be achieved, thereby improving J_{G_Si} greatly. Since the J_{G_Si} is determined by both $CsPbI_3$ layer thickness and Si bulk thickness, it fluctuates over a wide range from 17.06 mA/cm^2 (Si 40 μm, $CsPbI_3$ 2200 nm) to 22.25 mA/cm^2 (Si 210 μm, $CsPbI_3$ 400 nm).

Basically, the short-circuit current density (J_{sc}) of the entire two-terminal TSC reaches up to the lower one of the two subcells, bringing out the key problem of current matching. Figure 5 exhibits the J_{sc} of $CsPbI_3$/TOPCon TSCs and thickness of both $CsPbI_3$ layer and Si bulk for current density matching. When the $CsPbI_3$ layer is thinner than 600 nm, J_{sc} is unilaterally restricted by the $J_{G_CsPbI_3}$, indicating that even 40-μm Si is thick enough to match with $CsPbI_3$ layer. With the increase of $CsPbI_3$ layer thickness, the Si bulk should be thickened correspondingly. At present, the thickness of industrial used Czochralski (CZ) Si wafer is ∼ 180 μm, which is absolutely thick enough to match with a 2000-nm $CsPbI_3$ layer. According to previously published experimental data, the thickness of $CsPbI_3$ layer is usually less than 1000 nm as a result of crystallization quality, implying that the J_{sc} of the $CsPbI_3$/TOPCon TSC will be mainly determined by the thickness of $CsPbI_3$ layer. On the other hand, the bottom Si substrate has sufficient space to become thinner. The maximum J_{sc} can reach to 19.79 mA/cm^2 when the thickness of Si bulk and $CsPbI_3$ layer are 180 μm and 2180 nm, respectively.

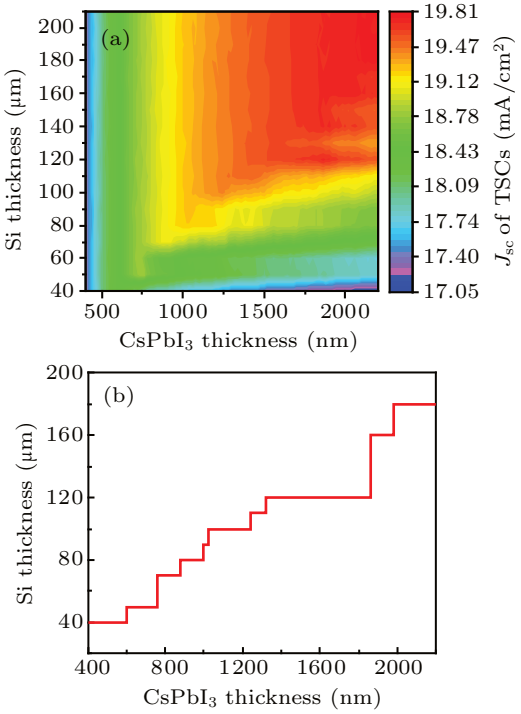


Fig. 5. (a) Short-circuit current density of $CsPbI_3$/TOPCon TSC and (b) matched thickness of $CsPbI_3$ layer and Si bulk.

2.4. Front TCO

The optimized structure of $CsPbI_3$/TOPCon TSC is shown in Fig. 6 according to the discussion above and its optical loss analysis. With the excellent bifacial texture and the matched thickness of $CsPbI_3$ layer and Si bulk, the whole optical loss can be reduced to 6.53 mA/cm^2. Of these various optical losses, parasitic absorption loss from the front ITO occupies the largest proportion, which reaches to 1.80 mA/cm^2. Therefore, restraining the parasitic absorption in the top TCO layer is an effective way to further enhance the optical performance of the $CsPbI_3$/TOPCon TSC.

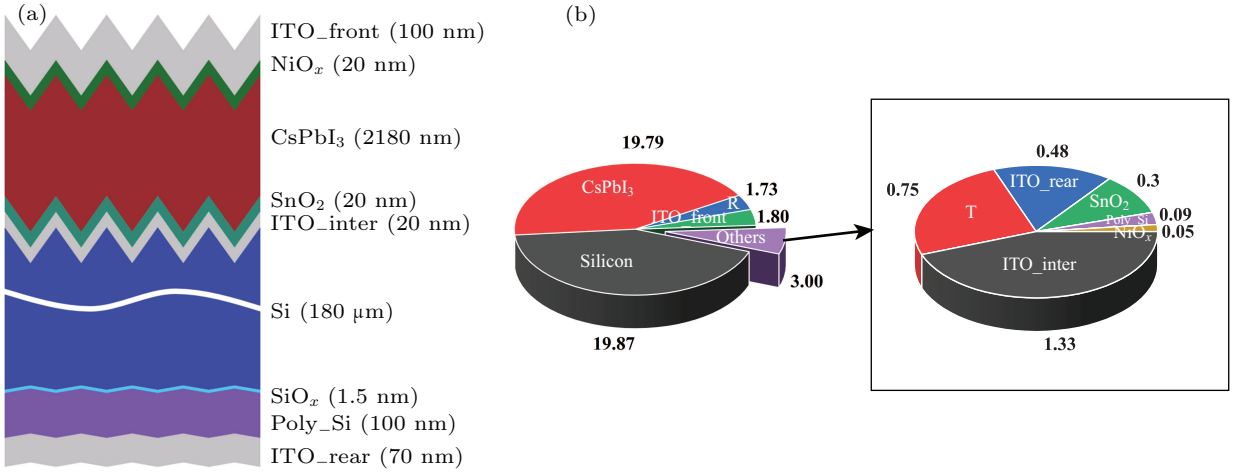


Fig. 6. Optical performance of optimized $CsPbI_3$/TOPCon TSC. (a) Simulated structure with optimized texture and absorber thickness; (b) photogenerated current density and optical losses of $CsPbI_3$/TOPCon TSC (in units mA/cm^2).

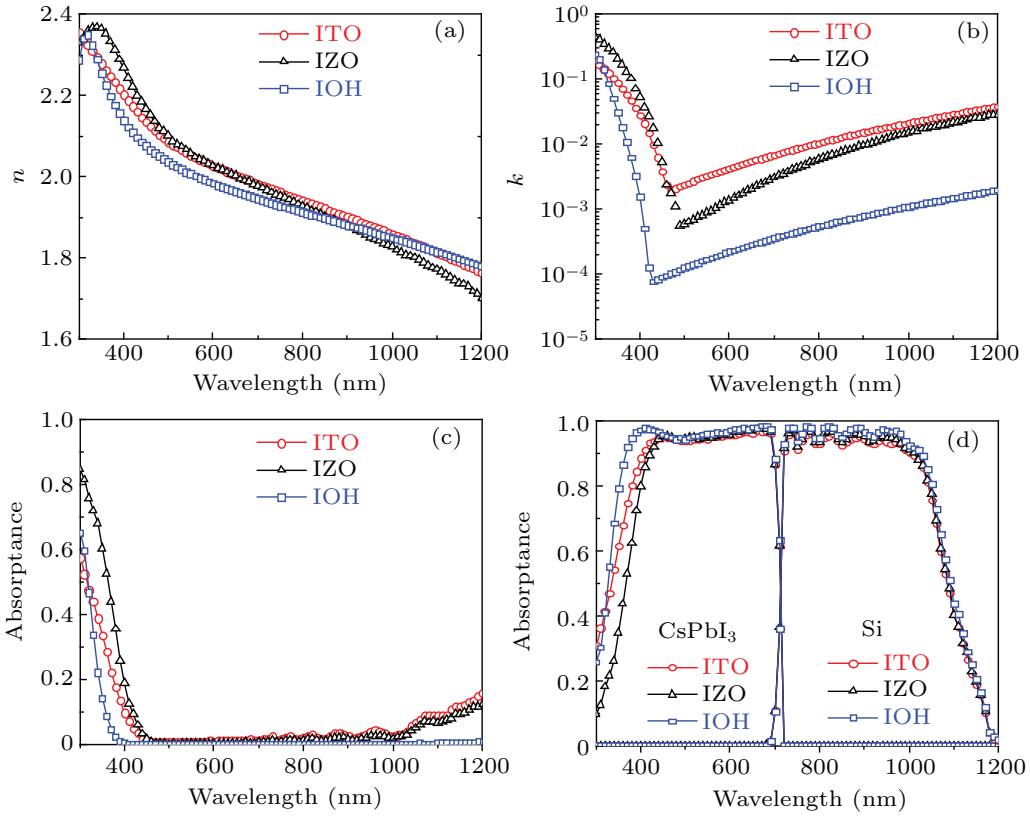


Fig. 7. Optical performances of different front TCOs, showing curves of wavelength dependent (a) n and (b) k of different TCO materials, (c) absorptance of front TCO layers, and (d) absorptance of $CsPbI_3$ layer and Si bulk.

An excellent front TCO needs to satisfy high conductivity, high transmittance and low parasitic absorption at the same time. To achieve a trade-off between transparency and conductivity, TCO is required to possess high electron mobility instead of high free carrier density.[42] In addition to the most shared ITO, indium zinc oxide (IZO) and IO:H are also key members of TCO, which possess lower near-infrared absorption due to their high carrier mobility and relatively low carrier density. The IO:H, in particular, offers high carrier mobility over 100 $cm^2 \cdot V^{-1} \cdot s^{-1}$ and a suitable carrier density on the order of 10^{20} cm^{-3}.[43–45] With the purpose to minimize the parasitic absorption loss from the front TCO, the optical performance of $CsPbI_3$/TOPCon TSC displayed in Fig. 6(a) was simulated with different front TCOs.

Figures 7(a) and 7(b) exhibit the refractive indexes n and extinction coefficients k of ITO, IZO, and IO:H (230-°C annealed), respectively.[29,46,47] Obviously, the k of IO:H is much lower than that of ITO and IZO in a wavelength range from 320 nm to 1200 nm, indicating a lower parasitic absorption with the same thickness. The IZO has a higher k in a range of 300 nm–460 nm, and a lower one in a range of 460 nm–1200 nm than the ITO. The absorption curves of these three TCOs are shown in Fig. 7(c). The IO:H presents the lowest parasitic absorption loss, that is 0.24 mA/cm^2, which is consistent with the extinction coefficient. Comparatively, the value for IZO just slightly decreases to 1.72 mA/cm^2 due to the substantial aggravation in a short wavelength range (300 nm–460 nm), although the parasitic absorption in a wide wavelength range is controlled. In this case, the $J_{G_CsPbI_3}$ and J_{G_Si} can be further improved to 20.27 mA/cm^2 and 20.51 mA/cm^2, respectively, when the front ITO is replaced by IO:H (Fig. 7(d)). Therefore, IO:H has the potential to be a preeminent material for the application in PVK/Si TSCs.

2.5. Device performance

After addressing all the optimization processes, the desirable architecture of the $CsPbI_3$/TOPCon TSC can be described as IO:H (100 nm)/NiO_x (20 nm)/$CsPbI_3$(2200 nm)/SnO_2 (20 nm)/ITO_inter (20 nm)/Si (170 μm)/SiOx (1.5 nm)/Poly_Si (100 nm)/ITO_rear (70 nm). We are able to accurately model the entire absorptance and external quantum efficiency (EQE) of the $CsPbI_3$/TOPCon TSC as illustrated in Fig. 8, which quantifies the optical losses in the integrated device. The best matched J_{sc} can reach to 20.27 mA/cm^2, which is determined primarily by the thickness of $CsPbI_3$ layer. After optimizing the front TCO, the front surface reflection and the parasitic absorption of interlayer ITO become the top two optical losses. Thus, introducing a suitable surface antireflective film and searching for a more promising interlayer material will be the next research directions for further improving the optical performance of the $CsPbI_3$/TOPCon TSCs.

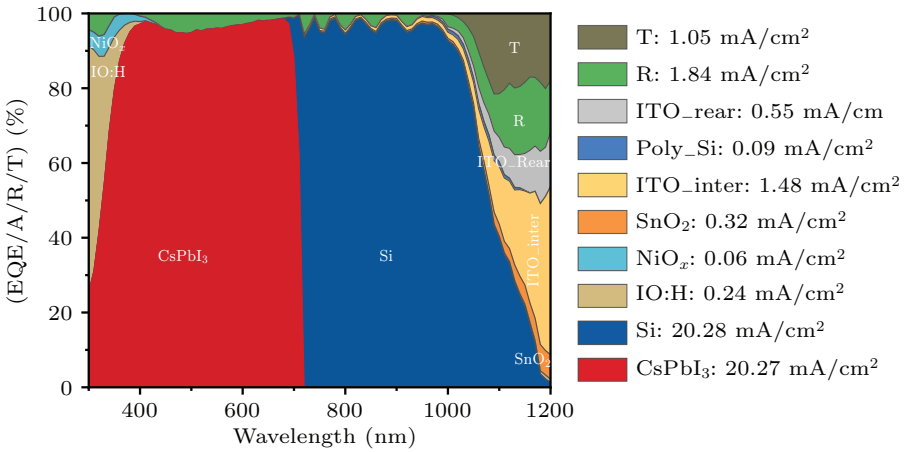


Fig. 8. Simulated EQE of subcells and optical losses (parasitic absorption, reflectance, and transmittance) of optimized $CsPbI_3$/TOPCon TSC, expressed as equivalent current densities.

To date, the efficiencies of champion $CsPbI_3$ solar cell and n-type TOPCon solar cells are 20.37% and 25.8% with V_{OC} of 1.198 V and 0.724 V, respectively.[16,48] We used these measured V_{oc} and the simulated J_G as input parameters to calculate the potential PCE of the $CsPbI_3$/TOPCon TSC. The model used to calculate the PCE is provided in Fig. S2 in Supporting information. We reconstructed the *J*–*V* curves of both subcells by calculating the implied voltage at each injected current, yielding a "pseudo" *J*–*V* curve for each subcell after shifting the *J*–*V* curve by the respective photogenerated current density J_G from the optimized $J_{G_CsPbI_3}$(20.27 mA/cm^2) and J_{G_Si} (20.28 mA/cm^2). The *J*–*V* curve of the TSC was obtained by applying the voltages to the subcells for each current density. The high *FF* (82.52%) calculated from the reconstructed *J*–*V* curve of TSC can be regarded as the maximum achievable value for this TSC if the electrodes and all charge selective layers are free of series resistance losses. Table 2 displays the simulated photovoltaic parameters of the subcells and the $CsPbI_3$/TOPCon TSC. A 31.78% PCE can be expected based on the favorable texture, matched current density and improved front TCO.

Table 2. Simulated photovoltaic parameters of $CsPbI_3$/TOPCon TSC.

Cells	J_{sc} (mA/cm^2)	V_{oc} (V)	*FF* (%)	*PCE* (%)
$CsPbI_3$ subcell	20.27	1.20	82.49	20.06
TOPCon subcell	20.28	0.70	82.71	11.74
Tandem	20.27	1.90	82.52	31.78

3. Conclusions

The optical performance of $CsPbI_3$/TOPCon two-terminal TSCs is simulated by the combination of ray-tracing and TMM. Compared with planar front surface, bifacial texture can significantly enhance the absorption of both $CsPbI_3$ layer and Si bulk due to the reduced front reflection triggered off by the front texture. Meanwhile, the b-IP textured TSC has a more superior photogenerated current density than b-UP textured counterpart. By reducing the bottom angle θ of rear-side inverted pyramid to 10.0°, the J_{G_Si} is further improved to 20.51 mA/cm^2, 2.9% higher than 0.0° and even 6.0% higher than typical 54.7°. A small θ can make a perfect trade-off between reflection and transmission of the light ranging from 1000 nm to 1200 nm, contributing to the enhancement of J_{G_Si}. When it comes to current matching, the thickness of $CsPbI_3$ layer and Si bulk should be well matched. Currently, $CsPbI_3$ films are usually thinner than 600 nm, thus a 40-μm thin Si is thick enough to match the photogenerated current density. For industrial CZ Si (∼ 180-μm thick), the J_{sc} of $CsPbI_3$/TOPCon TSC is restricted mainly by the thickness of $CsPbI_3$ layer. After optimizing the surface texture and matching the thickness values of photoactive layers, the parasitic absorption of front ITO becomes the largest optical loss. The IO:H will be a promising candidate for the front TCO with a minimized parasitic absorption loss as low as 0.24 mA/cm^2, considering its merits of high carrier mobility and relatively low carrier density. Finally, J_{sc} is achieved to be as high as 20.27 mA/cm^2, and a PCE over 30% can be expected.

Acknowledgements

The authors would like to thank Prof. Xiaolong Du and Dr. Yaoping Liu for the inspiring discussion.

Project supported by the National Natural Science Foundation of China (Grant Nos. 61904201 and 11875088) and the Guangdong Basic and Applied Basic Research Foundation, China (Grant No. 2019B1515120057).

References

[1] Yoshikawa K, Kawasaki H, Yoshida W, Irie T, Konishi K, Nakano K, Uto T, Adachi D, Kanematsu M, Uzu H and Yamamoto K 2017 *Nat. Energy* **2** 17032

[2] Richter A, Hermle M and Glunz S W 2013 *IEEE J. Photovoltaics* **3** 1184

[3] Almansouri I, Ho-Baillie A, Bremner S P and Green M A 2015 *IEEE J. Photovoltaics* **5** 968

[4] Burschka J, Pellet N, Moon S J, Humphry-Baker R, Gao P, Nazeeruddin M K and Grätzel M 2013 *Nature* **499** 316

[5] Meggiolaro D, Motti S G, Mosconi E, Barker A J, Ball J, Andrea Riccardo Perini C, Deschler F, Petrozza A and De Angelis F 2018 *Energy Environ. Sci.* **11** 702

[6] A K, K T, Y S and T M 2009 *J. Am. Chem. Soc.* **131** 6050

[7] Kim M, Jeong J, Lu H, *et al.* 2022 *Science* **375** 302

[8] Kim D, Jung H J, Park I J, Larson B W, Dunfield S P, Xiao C, Kim J, Tong J, Boonmongkolras P, Ji S G, Zhang F, Pae S R, Kim M, Kang S B, Dravid V, Berry J J, Kim J Y, Zhu K, Kim D H and Shin B 2020 *Science* **368** 155

[9] Mailoa J P, Bailie C D, Johlin E C, Hoke E T, Akey A J, Nguyen W H, McGehee M D and Buonassisi T 2015 *Appl. Phys. Lett.* **106** 121105

[10] NREL *Best Research-Cell Efficiency Chart* (accessed: May 2022)

[11] Bett A J, Schulze P S C, Winkler K M, Kabakli Ö S, Ketterer I, Mundt L E, Reichmuth S K, Siefer G, Cojocaru L, Tutsch L, Bivour M, Hermle M, Glunz S W and Goldschmidt J C 2020 *Prog. Photovoltaics Res. Appl.* **28** 99

[12] Richter A, Müller R, Benick J, Feldmann F, Steinhauser B, Reichel C, Fell A, Bivour M, Hermle M and Glunz S W 2021 *Nat. Energy* **6** 429

[13] Messmer C, Goraya B S, Nold S, Schulze P S C, Sittinger V, Schön J, Goldschmidt J C, Bivour M, Glunz S W and Hermle M 2021 *Prog. Photovoltaics Res. Appl.* **29** 744

[14] Zhang Y and Zhou H P 2019 *Acta Phys. Sin.* **68** 158804 (in Chinese)

[15] Eperon G E, Paternò G M, Sutton R J, Zampetti A, Haghighirad A A, Cacialli F and Snaith H J 2015 *J. Mater. Chem. A* **3** 19688

[16] Yoon S M, Min H, Kim J B, Kim G, Lee K S and Seok S Il 2021 *Joule* **5** 183

[17] Sutton R J, Filip M R, Haghighirad A A, Sakai N, Wenger B, Giustino F and Snaith H J 2018 *ACS Energy Lett.* **3** 1787

[18] Moreno M, Murias D, Martínez J, Reyes-Betanzo C, Torres A, Ambrosio R, Rosales P, Roca i Cabarrocas P and Escobar M 2014 *Sol. Energy* **101** 182

[19] Bush K A, Palmstrom A F, Yu Z J, *et al.* 2017 *Nat. Energy* **2** 1

[20] Hou Y, Aydin E, De Bastiani M, *et al.* 2020 *Science* **367** 1135

[21] Bush K A, Manzoor S, Frohna K, Yu Z J, Raiford J A, Palmstrom A F, Wang H P, Prasanna R, Bent S F, Holman Z C and McGehee M D 2018 *ACS Energy Lett.* **3** 2173

[22] Chen B, Yu Z J, Manzoor S, Wang S, Weigand W, Yu Z, Yang G, Ni Z, Dai X, Holman Z C and Huang J 2020 *Joule* **4** 850

[23] Wang Y, Yang L, Liu Y, Mei Z, Chen W, Li J, Liang H, Kuznetsov A and Xiaolong D 2015 *Sci. Rep.* **5** 10843

[24] Simeon C, Baker-Finch and K R M 2011 *Prog. Photovolt Res. Appl* **19** 406

[25] Hou F, Han C, Isabella O, Yan L, Shi B, Chen J, An S, Zhou Z, Huang W, Ren H, Huang Q, Hou G, Chen X, Li Y, Ding Y, Wang G, Wei C, Zhang D, *et al.* 2019 *Nano Energy* **56** 234

[26] Shi D, Zeng Y and Shen W 2015 *Sci. Rep.* **5** 16504

[27] Ba L, Liu H and Shen W 2018 *Prog. Photovoltaics Res. Appl.* **26** 924

[28] Al-Ashouri A, Köhnen E, Li B, *et al.* 2020 *Science* **370** 1300

[29] Holman Z C, Filipič M, Descoeudres A, De Wolf S, Smole F and Topič M, Ballif C 2013 *J. Appl. Phys.* **113** 013107

[30] Manzoor S, Häusele J, Bush K A, Palmstrom A F, Carpenter J, Yu Z J, Bent S F, Mcgehee M D and Holman Z C 2018 *Opt. Express* **26** 27441

[31] Yan W, Guo Y, Beri D, Dottermusch S, Chen H and Richards B S 2020 *Phys. Status Solidi - Rapid Res. Lett.* **14** 2000070

[32] Mazzarella L, Werth M, Jäger K, Jošt M, Korte L, Albrecht S, Schlatmann R and Stannowski B 2018 *Opt. Express* **26** A487

[33] Green M A 2008 *Sol. Energy Mater. Sol. Cells* **92** 1305

[34] Reiter S, Koper N, Reineke-Koch R, Larionova Y, Turcu M, Krügener J, Tetzlaff D, Wietler T, Höhne U, Kähler J D, Brendel R and Peibst R 2016 *Energy Procedia* **92** 199

[35] Byrnes S J 2016 arXiv: 1603.02720v5 [physics.comp-ph]

[36] GitHub Nanunanuk SMARTI: Ray tracing tool for solar cell and module optics (accessed: May 2022)

[37] Wang J M, Chen K, Xie W G, Shi T T, Liu P Y, Zheng Y F and Zhu R 2019 *Acta Phys. Sin.* **68** 158804 (in Chinese)

[38] Sahli F, Werner J, Kamino B A, Bräuninger M, Monnard R, Paviet-Salomon B, Barraud L, Ding L, Diaz Leon J J, Sacchetto D, Cattaneo G, Despeisse M, Boccard M, Nicolay S, Jeangros Q, Niesen B and Ballif C 2018 *Nat. Mater.* **17** 820

[39] Tang H, Liu Y, Chen Q, Wang Y, Chen W, Wu J, Zhao Y and Du X 2019 *ACS Appl. Electron. Mater.* **1** 2684

[40] Wang Y, Liu Y, Yang L, Chen W, Du X and Kuznetsov A 2017 *Nanoscale* **9** 907

[41] Macleod H A 1986 *Thin-Film Opt. Filters*, 3rd edn. (Bristol: Institute of Physics Pub) pp. 43–46

[42] Calnan S and Tiwari A N 2010 *Thin Solid Films* **518** 1839

[43] Battaglia C, Erni L, Boccard M, Barraud L, Escarré J, Sderstrm K, Bugnon G, Billet A, Ding L, Despeisse M, Haug F J, Wolf S De and Ballif C 2011 *J. Appl. Phys.* **109** 114501

[44] Koida T, Fujiwara H and Kondo M 2009 *Sol. Energy Mater. Sol. Cells* **93** 851

[45] Koida T, Kondo M, Tsutsumi K, Sakaguchi A, Suzuki M and Fujiwara H 2010 *J. Appl. Phys.* **107** 033514

[46] Jošt M, Köhnen E, Morales-Vilches A B, Lipovšek B, Jäger K, Macco B, Al-Ashouri A, Krč J, Korte L, Rech B, Schlatmann R, Topič M, Stannowski B and Albrecht S 2018 *Energy Environ. Sci.* **11** 3511

[47] Jiang Y, Feurer T, Carron R, Sevilla G T, Moser T, Pisoni S, Erni R, Rossell M D, Ochoa M, Hertwig R, Tiwari A N and Fu F 2020 *ACS Nano* **14** 7502

[48] Richter A, Benick J, Feldmann F, Fell A, Steinhauser B, Polzin J I, Tucher N, Murthy J N, Hermle Ma and Glunz S W 2019 36*th Eur. Photovolt. Sol. Energy Conf. Exhib.* September 9–13, 2019, Marseille, France, p. 13